QWIP DESIGN: AN APPROACH USING THE TRANSFER MATRIX METHOD TO CALCULATE THE BOUND STATES IN VALENCE AND CONDUCTION BAND

Ricardo A. Tavares Santos*, Fábio Durante P. Alves*, Christian G. R. Taranti**, Jayr de Amorim Filho*, Gamani Karunasiri***.

*Instituto Tecnológico de Aeronáutica, **Instituto de Aeronáutica e Espaço, ***Naval Postgraduate School

Abstract: *This work presents a technique to calculate bound states in both conduction and valence band in complex quantum well structures. QW physics and the Transfer Matrix (TM) formalism are discussed. Analytical solutions to solve 2x2 Hamiltonians, as well as numerical results from TM are presented too. The theoretical data are compared with results from the literature and measurements from actual device. The results show good agreement between all compared data, indicating that TMM has a great potential to be used in QWIP design.*

Key words: *quantum wells infrared photodetectors, transfer matrix method, design.*

I. INTRODUCTION

The design of photodetectors capable to detect different bands simultaneously with high sensitivity have found in quantum wells infrared photodetectors a good alternative. To be able to design such devices, it is necessary to use theoretical approaches with enough accuracy to estimate the confined quantum wells (QW) energy levels and its respective wave functions (the eigenvalues and the eigenfunctions). Accuracy is very important to allow the estimation of the wavelength detected by a device using interband and intersubband transitions

This work presents an approach to calculate the quantum wells confined energy levels and its wave functions in both valence and conduction bands using the Transfer Matrix Method (TMM). This is a versatile method in obtaining the transmission coefficient, the energy states and the corresponding wave functions of a QW structure with any potential profile. In this technique, the structure can be divided in N slices describing parts of the device, resulting in a matrix multiplication describing the propagation of a plane wave across the whole multilayer structure.

The work starts with a description of the basics of QW physics and the TMM formalism. After, the analytical solution of the used Hamiltonian is described. The numerical estimation and the comparison with the literature data and measurements are shown in the fourth part.

II. QUANTUM WELLS PHYSICS AND TMM

It is necessary discuss some basic aspects about the physics of QW to understand how to find the confined energy levels and what Hamiltonians were used to calculate them. Also, will be described the mathematical tool used to solve the employed Hamiltonians.

1. QW physics

Heterostructures for QW devices are constructed in three forms: the single junction structures, often referred as simple heterostructures, the double junction structures, mostly referred as QW and multi-junction structures, called superlattices. These are show in Figure 1. Electron states in the structures are evaluated by assuming that the bulk and band structures remain applicable for the constituents, even though the physical dimension in one or more directions may be comparable to the lattice constant. Electron states in the structure are obtained by solving the wave equation for the potential distributions in the structure by using the bulk physical constants and by applying the known effective-mass approximation and the suitable boundary conditions (1).

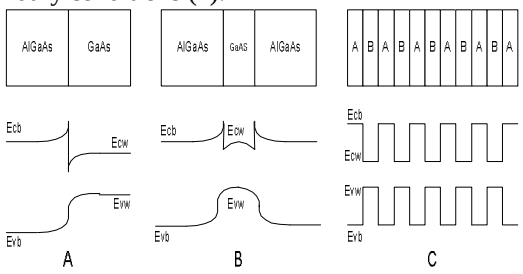

Figure 1: Heterostructures in QW. (A) single junction; (B) double junction ; (C) multi-junction (superlattice) **(1)**.

In QW, the potential profile is defined considering the joining of the band off-set of each constituent alloy. In this way, quantized energy levels are allowed confined in the wells, while continuum states are possible outside. Figure 2 shows a representation of potential profile of a multiple quantum wells (MQW).

In the figure, the barriers and the wells are in different colors highlighting their band gaps defined by E_{gB} and E_{gW}, respectively. CBO and VBO stand for conduction and valence band off-sets, E_c and E_v the confined energy levels, z is the growing axis and V is energy axis as a function of z.

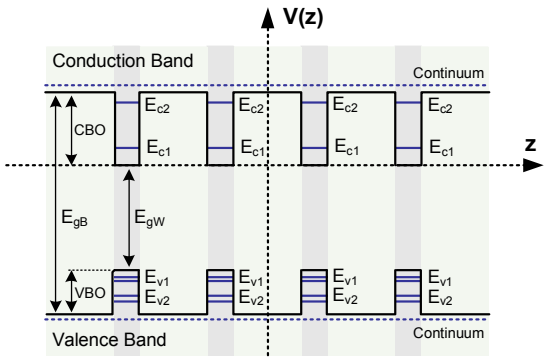

Figure 2: potential profile of a multiple quantum wells **(2)**.

In the effective mass approximation, the Schrödinger equation reads:

$$-\nabla\frac{\hbar^2}{2m}\nabla\psi + V\psi = E\psi, \qquad \text{Eq. 1}$$

where m is the effective mass and *V* is the potential. Here, the potential is due to three fonts: the potential from the alloys band off-set, the potential due to an external applied bias, necessary to operate photoconductive photodetectors, and the potential due to charge distribution. The total potential can be described as:

$$V_{total} = V_{Eg} + V_{bias} + \mathrm{V}\rho. \qquad \text{Eq. 2}$$

There are many ways to calculate the bandstructure for semiconductors. This work will employ **k.p** method because this method provides an accurate description of the medium evaluated and it is simple to implent. In addition, using its simplest form is possible to describe the conduction and valence band in same way (2). In this case, if the *z*-axis is chosen as the growth direction, the wavefunction is separable into a lateral (*x*-*y* plane) part ψ_{xy} and a z part ψ_z. The lateral part is simply a plane wave with kinetic energy $E_{||}$ (E_{xy}). For the *z* part, ψ_z is a solution of

$$-\frac{\mathrm{d}}{\mathrm{d}z}\frac{\hbar^2}{2m}\frac{\mathrm{d}}{\mathrm{d}z}\psi(z) + V\psi(z) = E_{\perp}\psi(z), \qquad \text{Eq. 3}$$

such that $E = E_{||} + E_{\perp}$. Taking into account that *m=m(z)* for different barrier and well materials, the operator $\frac{d}{dz}$ does not commute with $\frac{1}{m}$. Then Eq. 3 requires ψ_z and $\frac{1}{m}\frac{d\psi(z)}{dz}$ to be continuous at the interfaces between different materials (3). In this work, will be considered that there is no energy dispersion in the *x*-*y* plane, so $E_{||}=0$ (special case with $k_x=k_y=0$). Finally, the probability interpretation of the wavefunction requires the normalization condition for the bound states potential and the solution to Eq. 3 has the mathematically form:

$$\psi(z) = Ae^{ik_z z} + Be^{-ik_z z}. \qquad \text{Eq. 4}$$

The electronic wave functions that satisfy the Schrodinger equation with a periodic lattice potential in a bulk crystal are given by Bloch's theorem:

$$\psi(z) = e^{ik_z z}u_{nk}(z). \qquad \text{Eq. 5}$$

The cell-periodic Bloch functions $u_{nk}(z)$ depend on the band index *n* and the envelope function wave vector *k*. The wave functions $\psi(z)$ form a complete set of states as do the wave functions based on Bloch functions at any other wave vector, including the wave vectors at special points in the Brilloin Zone. In treating the optical and electronic properties of direct gap semiconductors, it is natural to consider the zone-center Γ-point Bloch functions $u_{nk}(z)$ for the used wave function expansions. From now, the reference to the *k=0* index, was dropped for these functions.

2. Analytical Solution of the Hamiltonian

The total Hamiltonian H_0 for the valence band can be written in two parts. The first part depends on the components of the wave vector (k_x, k_y, k_z). The second part depends on strain components ε_{xy}, with a one-to-one correspondence between terms k_xk_y and ε_{xy} and their coefficients (4):

$$H_0 = H + H_{\varepsilon}, \qquad \text{Eq. 6}$$

where

$$H_0 = -\begin{bmatrix} P_t+Q_t & -S_t & R_t & 0 \\ -S_t^{\dagger} & P_t-Q_t & 0 & R_t \\ R_t^{\dagger} & 0 & P_t-Q_t & S_t \\ 0 & R_t^{\dagger} & -S_t^{\dagger} & P_t+Q_t \end{bmatrix} \begin{matrix} |\frac{3}{2},\frac{3}{2}\rangle \\ |\frac{3}{2},\frac{1}{2}\rangle \\ |\frac{3}{2},-\frac{1}{2}\rangle \\ |\frac{3}{2},-\frac{3}{2}\rangle \end{matrix} \qquad \text{Eq. 7}$$

and

$$\begin{aligned} P_t &= P + P_{\varepsilon}, \\ Q &= Q + Q_{\varepsilon}, \\ R_t &= R + R_{\varepsilon}, \\ S_t &= S + S_{\varepsilon}. \end{aligned} \qquad \text{Eq. 8}$$

The expressions for the above matrix elements are

$$\begin{aligned} P &= \left[\frac{\hbar\gamma_1}{(2m)}\right](k_x^2 + k_y^2 + k_z^2), \\ Q &= \left[\frac{\hbar\gamma_2}{(2m)}\right](k_x^2 + k_y^2 - 2k_z^2), \\ R &= -\left[\frac{\hbar\gamma_2}{(2m)}\right]\sqrt{3}(k_x^2 - k_y^2) \\ &\quad + i\left[\frac{\hbar\gamma_3}{(2m)}\right]2\sqrt{3}k_xk_y, \\ S &= \left[\frac{\hbar\gamma_3}{(2m)}\right]2\sqrt{3}(k_x - ik_y)k_z; \end{aligned} \qquad \text{Eq. 9}$$

$$\begin{aligned} P_{\varepsilon} &= -D_d(\varepsilon_{xx} + \varepsilon_{yy} + \varepsilon_{zz}), \\ Q_{\varepsilon} &= \frac{D_d}{3}(\varepsilon_{xx} + \varepsilon_{yy} - 2\varepsilon_{zz}), \\ R_{\varepsilon} &= -\frac{D_u}{3}\sqrt{3}(\varepsilon_{xx} + \varepsilon_{yy}) - i\left[\frac{D'_u}{3}\right]\varepsilon_{xy}, \\ S &= \frac{D'_u}{3}2\sqrt{3}(\varepsilon_{xz} - i\varepsilon_{yz}). \end{aligned} \qquad \text{Eq. 10}$$

The correspondence is

$$\begin{aligned} \frac{\hbar\gamma_1}{(2m)} \leftrightarrow -D_d \equiv a_v, \qquad \frac{\hbar\gamma_2}{(2m)} \leftrightarrow \frac{D_u}{3}, \\ \frac{\hbar\gamma_3}{(2m)} \leftrightarrow \frac{D'_u}{3}, \\ k_ik_j \leftrightarrow \varepsilon_{ij},\ i,j = x,y,z. \end{aligned} \qquad \text{Eq. 11}$$

The basis functions are

$$
\begin{aligned}
|\tfrac{3}{2},\tfrac{3}{2}\rangle &= -\frac{1}{\sqrt{2}}|(X+iY)\uparrow\rangle,\\
|\tfrac{3}{2},\tfrac{1}{2}\rangle &= -\frac{1}{\sqrt{6}}|(X+iY)\downarrow\rangle + \sqrt{\frac{2}{3}}|Z\uparrow\rangle,\\
|\tfrac{3}{2},-\tfrac{1}{2}\rangle &= \frac{1}{\sqrt{6}}|(X-iY)\uparrow\rangle + \sqrt{\frac{2}{3}}|Z\downarrow\rangle,\\
|\tfrac{3}{2},-\tfrac{3}{2}\rangle &= \frac{1}{\sqrt{2}}|(X-iY)\downarrow\rangle.
\end{aligned}
\qquad \text{Eq. 12}
$$

To make the calculation procedure easier, it is necessary to block-diagonalize the previous Hamiltonian in a 2x2 matrices. So, it was used a unitary transformation. The strain due to lattice constant difference was also considered. After this procedure, the Hamiltonian is re-written as (4):

$$H = \begin{bmatrix} H^U & 0 \\ 0 & H^L \end{bmatrix}, \qquad \text{Eq. 13}$$

where

$$
\begin{aligned}
H^U &= -\begin{bmatrix} P+Q+\zeta & \tilde{R} \\ \tilde{R}^\dagger & P-Q-\zeta \end{bmatrix} \\
&\quad + D_d(\varepsilon_{xx}+\varepsilon_{yy}+\varepsilon_{zz}),\\
H^L &= -\begin{bmatrix} P-Q-\zeta & \tilde{R} \\ \tilde{R}^\dagger & P+Q+\zeta \end{bmatrix} \\
&\quad + D_d(\varepsilon_{xx}+\varepsilon_{yy}+\varepsilon_{zz})
\end{aligned}
\qquad \text{Eq. 14}
$$

with $\tilde{R} = |R| - i|S|$; P,Q,R, and S defined in Eq. 9. For the strained-lattice case, the strain is given by

$$
\begin{aligned}
\varepsilon_{xx} = \varepsilon_{yy} &= \frac{a_0 + a(x)}{a_0} = \varepsilon,\\
\varepsilon_{zz} &= -2\frac{C_{12}}{C_{11}}\varepsilon,\\
\varepsilon_{xy}&=\varepsilon_{xz}=\varepsilon_{zy}=0.
\end{aligned}
\qquad \text{Eq. 15}
$$

In the conduction band, the Hamiltonian is given by

$$
\begin{aligned}
H_C &= \frac{\hbar^2}{2m_n^*}\left(k_x^2+k_y^2+k_z^2\right)\\
&\quad + C_1\left(\varepsilon_{xx}+\varepsilon_{yy}+\varepsilon_{zz}\right),
\end{aligned}
\qquad \text{Eq. 16}
$$

where m_n^* is the electron effective mass and C_1 is the deformation potential for the conduction band. Some definitions are important:

$$
\begin{aligned}
a_v &= -D_d, \qquad a = C_1 + a_v,\\
\delta E_{sh} &= -2b\left[1+\frac{C_{12}}{C_{11}}\right]\varepsilon,\\
\zeta &= \frac{1}{2}\delta E_{sh}.
\end{aligned}
\qquad \text{Eq. 17}
$$

The reference [1] suggestion was considered and C_1=2a/3, and a_v=a/3, were assumed.

Recalling the Hamiltonian in the valence band, since the hydrostatic stress component $D_d(\varepsilon_{xx}+\varepsilon_{yy}+\varepsilon_{zz})$ only introduces a shift in the valence band, this term will be ignored temporally. It is important to state that the hole energy $\bar{E}$ is taken to be positive downward: $\bar{E} = -E$. The solutions for the eigenvalues and corresponding eigenvectors of the upper Hamiltonian are the following (4):

1. For the Heavy hole

$$
\begin{aligned}
\bar{E} &= P - [(Q+\zeta)^2 + \tilde{R}\tilde{R}^\dagger]^{\frac{1}{2}},\\
\begin{bmatrix} F_{1HH} \\ F_{2HH} \end{bmatrix} &= \begin{bmatrix} -(Q+\zeta) + [(Q+\zeta)^2 + \tilde{R}\tilde{R}^\dagger]^{\frac{1}{2}} \\ -\tilde{R}^\dagger \end{bmatrix}\\
&= \begin{bmatrix} P-(Q+\zeta)-\bar{E} \\ -\tilde{R}^\dagger \end{bmatrix}.
\end{aligned}
\qquad \text{Eq. 18}
$$

2. For the Light hole

$$
\begin{aligned}
\bar{E} &= P + [(Q+\zeta)^2 + \tilde{R}\tilde{R}^\dagger]^{\frac{1}{2}},\\
\begin{bmatrix} F_{1LH} \\ F_{2LH} \end{bmatrix} &= \begin{bmatrix} \tilde{R} \\ -(Q+\zeta) + \left[(Q+\zeta)^2 + \tilde{R}\tilde{R}^\dagger\right]^{\frac{1}{2}} \end{bmatrix} =\\
&\quad \begin{bmatrix} \tilde{R} \\ \bar{E}-P-(Q+\zeta) \end{bmatrix}.
\end{aligned}
\qquad \text{Eq. 19}
$$

There are other alternatives forms and solutions for both, upper and lower Hamiltonians, and ζ can be positive, if the strain is a compression, or positive, if the strain is a tension.

The wave functions can be written as (before normalization) (4)

$$
\begin{aligned}
\psi_{HH}(r) &= F_{1HH}e^{ik.r}|1\rangle + F_{2HH}e^{ik.r}|2\rangle,\\
\psi_{HH}(r) &= \begin{bmatrix} F_{1HH} \\ F_{2HH} \end{bmatrix} e^{ik.r}
\end{aligned}
\qquad \text{Eq. 20}
$$

for heavy hole, and

$$
\begin{aligned}
\psi_{LH}(r) &= F_{1LH}e^{ik.r}|1\rangle + F_{2LH}e^{ik.r}|2\rangle,\\
\psi_{LH}(r) &= \begin{bmatrix} F_{1LH} \\ F_{2LH} \end{bmatrix} e^{ik.r}
\end{aligned}
\qquad \text{Eq. 21}
$$

for light hole. Similar expressions hold for solutions using the other two bases $|3\rangle$ and $|4\rangle$ from the lower Hamiltonian.

As cited in (4): The classification of heavy hole is mainly from the fact that at $k=0$, the wave function has only a component along the basis $|1\rangle$ for the upper Hamiltonian and $|4\rangle$ for the lower. These bases are linear combinations of $|3/2,\pm 3/2\rangle$ basis functions. The other bases have a similar behave. Since the general valence-band structure of a strained semi-conductor is distorted due to the effects of strains, it is natural to classify the heavy- and light-hole bands by their basis functions at $k=0$. In this way, at $k_x=k_y=0$, $E=-\zeta<0$ (HH), and $E=+\zeta>0$ (LH); along the k_z direction, it is obtained for both compression and tension,

$$
\begin{aligned}
E &= -\frac{\hbar^2}{2m}(\gamma_1 - 2\gamma_2)k_z^2 - \zeta\ (HH),\\
E &= -\frac{\hbar^2}{2m}(\gamma_1 + 2\gamma_2)k_z^2 + \zeta\ (LH).
\end{aligned}
\qquad \text{Eq. 22}
$$

3. The Transfer Matrix Method

The next figure illustrates a heterostructure with the notation used in the work. The *L* and *R* domains are

often though not necessarily always semi-infinite, while the inner domains are finite ($m=1,\ldots,n$). The entire middle region will be labeled M (from z_l to z_r).

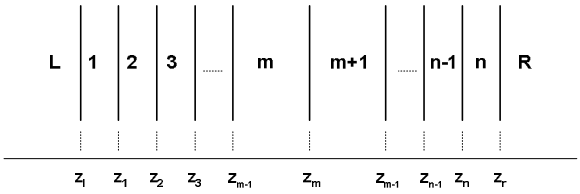

Figure 3: the heterostructure using the notation to be used in the TMM (5).

To calculate the eigenenergies and the eigenvalues for a heterostructure as showed above, it is necessary to correlate the different domains using the imposed boundary conditions. The TM is a method to correlate different domains following the imposed boundary conditions to match the solutions.

General Definitions

The Transfer Matrix (TM) can be obtained by some numerical procedure equivalent to a numerical integration. The implementation admits different forms and thus different objects are defined in the literature and the term TM is used to denote these different objects. To denote these effects and the necessity to represent the medium described, the symbol α is introduced as a domain symbol, which corresponds to L or R for barriers and M for the well (5).

By the previous assumption, α is considered as a domain of a certain material and $\mathbb{F}(\alpha: z)$ is described as being a solution of the differential system describing the corresponding medium α. The notation $(\alpha: z)$ denotes any point z in the medium. Now, three different objects can be defined, following the classification suggested by (5):

Full Transfer Matrix (FTM) denoted $M(\alpha: z, z_0)$. This transfers amplitudes and derivatives from z to z_0:

$$\begin{vmatrix} \mathbb{F}(\alpha: z) \\ \mathbb{F}'(\alpha: z) \end{vmatrix} = M(\alpha: z, z_0) \begin{vmatrix} \mathbb{F}(\alpha: z_0) \\ \mathbb{F}'(\alpha: z_0) \end{vmatrix}. \quad \text{Eq. 23}$$

where $\mathbb{F}$ is an N-vector, and M is an 2Nx2N matrix.

Associated Transfer Matrix (ATM) denoted $T(\alpha: z, z_0)$. This transfers the amplitude $\mathbb{F}$ and the linear differential form $\mathbb{A}$. Thus:

$$\mathbb{A}(z) = B(z)\frac{d\mathbb{F}(z)}{dz} + P(z)\mathbb{F}(z)$$

$$\begin{vmatrix} \mathbb{F}(\alpha: z) \\ \mathbb{A}'(\alpha: z) \end{vmatrix} = T(\alpha: z, z_0) \begin{vmatrix} \mathbb{F}(\alpha: z_0) \\ \mathbb{A}'(\alpha: z_0) \end{vmatrix} \quad \text{Eq. 24}$$

$$\mathbb{A}(\alpha: z) = P(\alpha: z)\mathbb{F}(\alpha: z) + B(\alpha: z)\mathbb{F}'(\alpha: z)$$

Coefficient Transfer Matrix (CTM) denoted $K(\alpha', \alpha)$. Note that this refers to a substantially different situation. In this case two different domains are related. And now, the media α can be assumed, while α' can be described analytically because the basis amplitudes are known: $\mathbb{F}_j(\alpha: z)$ and $\mathbb{F}_j(\alpha: z')$. Hence:

$$\mathbb{F}(\alpha: z) = \sum_j a_j(\alpha)\mathbb{F}_j(\alpha: z); \quad \text{Eq. 25}$$

$$\mathbb{F}(\alpha': z) = \sum_j a_j(\alpha')\mathbb{F}_j(\alpha': z).$$

Summations over j run always from 1 to 2N. Let $a(\alpha)$ be the vector formed by the $a_j(\alpha)$. Then

$$a(\alpha') = K(\alpha', \alpha)a(\alpha). \quad \text{Eq. 26}$$

The $K(\alpha', \alpha)$ transfers the set of coefficients a_j from domain α to domain α'.

Now, the structure should be viewed by the next figure instead of Figure 3.

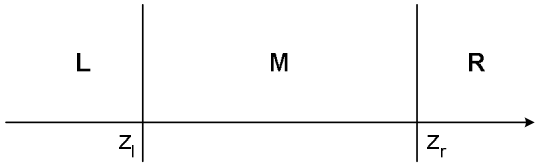

Figure 4: a heterostructure where M, the middle domain, can be anything, simple or complex (5).

The labels L and R have the same meaning and all included in the middle region M can be described by a simple ATM T. Thus, can be written

$$\psi(z) = \begin{cases} \mathbb{Q}(L: z)a(L); \ for\ z \le z_l \\ T(z, z_l)\psi(z_l); \ for\ z_l \le z \le z_r \\ \mathbb{Q}(R: z)a(R); \ for\ z \ge z_r \end{cases}. \quad \text{Eq. 27}$$

Since ψ is continuous at z_l and z_r:

$$\mathbb{Q}(R: z)a(R) = T(z, z_l); \quad \text{Eq. 28}$$

$$a(R) = K(R, L)a(L),$$

whence

$$K(R, L) = [\mathbb{Q}(R: z_r)]^{-1}T(z, z_l)\mathbb{Q}(R: z_l) \quad \text{Eq. 29}$$

which yields a expression for the CTM obtained from the T scheme. Where

$$\mathbb{Q}(z) = |\psi_1(z)\ \psi_2(z)\ \ldots\ \psi_{2N}(z)|, \quad \text{Eq. 30}$$

$$T(z, z_0) = \mathbb{Q}(z)\mathbb{Q}(z_0)^{-1}$$

$$= \begin{vmatrix} T_{AA}(z, z_0) & T_{AD}(z, z_0) \\ T_{DA}(z, z_0) & T_{DD}(z, z_0) \end{vmatrix} \quad \text{Eq. 31}$$

$$T(z_0, z_0) = I$$

In this case A means amplitude and D derivative, and *T* comes from the ATM definition.

Now, some K matrix characteristics may be listed, also as suggested by (5):

- K depends on the basis;
- If $z_0 < z_1 < z_2$, then K has the chain property

$$T(z_2, z_0) = T(z_2, z_1)T(z_1, z_0) \quad \text{Eq. 32}$$

- If L/R domain were choose as a basis, in the T scheme, which is canonical at z_l/z_r, then $K(R,L) = T(z_r, z_l)$.
- The determinant of $K(R,L)$ depends on the differential system and on the basis employed.
- If there is no M region, L and R match at $z_r=z_l=z$, then, $T(z_r, z_l) = I_{2N}$ and

$$K(R,L) = [\mathbb{Q}(R:z)]^{-1}\mathbb{Q}(R:z), \quad \text{Eq. 33}$$

It is important to note that CTM relates domains, while the FTM and ATM relate local positions.

To solve the problem of finding the confined energy levels in QW structures the CTM is employed.

III. BOUND STATES CALCULATIONS USING TMM

For a strained QW, the upper Hamiltonian described in equation Eq**.** 14 has the form (4)

$$H = -\left[\begin{bmatrix} P+Q+\zeta & \widetilde{R} \\ \widetilde{R}^{\dagger} & P-Q-\zeta \end{bmatrix} + V_s(z)\right], \quad \text{Eq. 34}$$

where should be defined

$$V_s = \begin{cases} 2a_v\left[1-\frac{C_{12}}{C_{11}}\right]\varepsilon \ \ (well) \\ \Delta E_v \ \ (barrier) \end{cases}, \quad \text{Eq. 35}$$

and ζ being zero in the barriers regions, assuming the barrier much thicker than the well, so that the elastic strain exists only inside the well. To estimate the gap energy for the heterostructure, the Varshini's equations were used with alloys parameters given in (6), and for the split between the conduction and the valence band was used the known rate of 65:35, respectively (6), for GaAs/AlGaAs interfaces.

The solutions for the upper Hamiltonian can be obtained replacing k_z by $-i\frac{\delta}{\delta z}$ and solving the effective mass equation (4)

$$\left[H\left[-i\tfrac{\delta}{\delta z}\right] - E\right]\psi(z) = 0. \quad \text{Eq. 36}$$

To solve the lower Hamiltonian, the same procedure can be used. So, the final Hamiltonian expression can be described as

$$H = -\begin{bmatrix} \frac{\hbar^2}{2m_0}(\gamma_1+2\gamma_2)k_z^2+\zeta & 0 \\ 0 & \frac{\hbar^2}{2m_0}(\gamma_1+2\gamma_2)k_z^2-\zeta \end{bmatrix} \quad \text{Eq. 37}$$

$$-V_s(z).$$

In this case, due to the strain, the heavy and light holes are decoupled. Solving the expression for each layer of the heterostructure, the wave function resulted can be written as

$$\psi_j(z) = A_j e^{ik_{jz}(z-z_j)} + B_j e^{-ik_{jz}(z-z_j)} \quad \text{Eq. 38}$$

For both heavy and light holes inside the interval (z_{j-1}, z_j) for $z_{j-1} < z < z_j$, where j means the jth region. The parameters A_j and B_j are determined using the fact of that the functions ψ and $\frac{d}{dz}\frac{\psi}{m_0}$ are continuous at the positions $z=z_j$.

Using these boundary conditions and the CTM, having A_j and B_j as the coefficients, the following expression can be proposed

$$\begin{pmatrix} A_{j+1} \\ B_{j+1} \end{pmatrix} = K_{j+1,j}\begin{pmatrix} A_j \\ B_j \end{pmatrix} \quad \text{Eq. 39}$$

where the matrix *K* can be obtained using the Eq. 26 in its evaluated form proposed by (5):

$$K_{j+1,j} = \begin{vmatrix} \Lambda_j(j:z_s)g_{j+1}(j+1:z_s) & \Lambda_j(j:z_s)g_{j+1}(j+1:z_s) \\ \Lambda_j(j:z_s)g_{j+1}(j+1:z_s) & \Lambda_j(j:z_s)g_{j+1}(j+1:z_s) \end{vmatrix} \quad \text{Eq. 40}$$

where $g_j(z)$ is a scalar function and $\Lambda_j(z)$ is a vector function of z which was chosen to vary smoothly as possible. So, the function $\Lambda_j(j:z_s)$ can brings the characteristics of the medium and the function $g_{j+1}(j+1:z_s)$ is a propagation matrix. Using the vector function as suggest by (3) and (4), the equation Eq**.** 40 can be written as

$$K_{j+1,j} = \frac{1}{2}\begin{vmatrix} (1+\alpha_j)e^{ik_{j+1}l_{j+1}} & (1-\alpha_j)e^{ik_{j+1}l_{j+1}} \\ (1-\alpha_j)e^{-ik_{j+1}l_{j+1}} & (1+\alpha_j)e^{-ik_{j+1}l_{j+1}} \end{vmatrix} \quad \text{Eq. 41}$$

Where $l_{j+1} = z_{j+1} - z_j$ and $\alpha_j = \frac{k_j m_{j+1}}{k_{j+1} m_j}$. In the case of heavy holes, $m_j = \frac{m_0}{(\gamma_1-2\gamma_2)}$, and for light holes, $m_j = \frac{m_0}{(\gamma_1+2\gamma_2)}$. At this point, it is important define k_z:

$$k_z^2 = \frac{1}{\frac{\hbar^2}{2m_0}(\gamma_1-2\gamma_2)}[E-\zeta-V_s(z)] \quad \text{Eq. 42}$$

for heavy holes, and

$$k_z^2 = \frac{1}{\frac{\hbar^2}{2m_0}(\gamma_1+2\gamma_2)}[E+\zeta-V_s(z)] \quad \text{Eq. 43}$$

for light holes.

According to TM theory, Eq. 39 represents a recursion relation between the coefficients A_j and B_j associated with adjacent intervals. The interaction gives raise an equation of the form

$$\begin{pmatrix} A_N \\ B_N \end{pmatrix} = K\begin{pmatrix} A_0 \\ B_0 \end{pmatrix}, \quad \text{Eq. 44}$$

Where, $K = K_{N,N-1}K_{N,N-2}\ldots K_{1,0}$. Knowing the behavior of a wave function from left to right, it is possible to deduce the coefficients *A* and *B*. Considering a heterostructure composed by only three layers (as a single square quantum well) and a wave function propagating from left to right, there should be an asymptotic growing in the first layer (left side) and an asymptotic decaying in the third layer (right side). Logically, the wave function doesn't reach the infinite in the final of the first layer, neither reaches the zero value in the last layer. It goes to a real value imposed by the boundary conditions in the junction as described before. These behaviors impose $A_0=0$ and $B_n=1$ for equation Eq**.** 38.

Analyzing the K matrix, it can be divided in

$$K = \begin{bmatrix} m11 & m12 \\ m21 & m22 \end{bmatrix}. \qquad \text{Eq. 45}$$

So, for bound states, E<V, and according to Eq. 38, Eq. 42 and Eq. 43, and the values assumed by A_0 and B_n in Eq. 44, *m22=0*, such that the associated subband energies can be calculated by finding the zeroes of m22(E).

For the conduction band, the procedure related can be repeated, replacing the heavy and light holes effective mass by the electron effective mass in each medium, making $\zeta == 0$ and also replacing *Ev* for *Ec* where

$$V_e = \begin{cases} 2C_1\left[1 - \dfrac{C_{12}}{C_{11}}\right]\varepsilon \ (well) \\ \Delta E_c \ (barrier) \end{cases}, \qquad \text{Eq. 46}$$

where $C_1=2a/3$.

IV. NUMERICAL RESULTS FOR QW STRUCTURES

To calculate the eigenenergies and the eigenfunctions it is necessary to divide the potential profile in slices to be used by the TMM. When the structure is formed by layers with constant potential, such as ideal square wells, only one slice is necessary to describe each layer. When an external electric field is applied it is necessary to evaluate how many slices should be employed to describe each semiconductor layer. Stronger field requires more slices to better describes the potential profile. It is also true for arbitrary potentials. The next figure shows the comparison between the original potential with an applied external bias and the modified potential profile used by the TMM. In each slice of the TMM, the potential is constant, indicating, as said before, for stronger electric fields more slices are necessary to simulate the original potential profile.

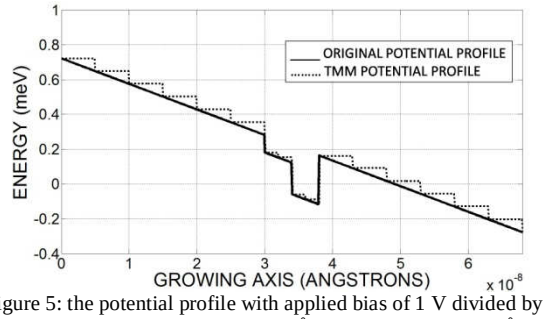

Figure 5: the potential profile with applied bias of 1 V divided by the TMM using slices with length of 50 Å in the barriers and 20 Å in the well.

To calculate the bound states using the TMM, the energy level must vary in the range of the barrier height. From the bottom of the well to the top of the well. For each value of energy, the TMM calculates the respective wave vector and other parameters for each slice inside each barrier and well layers, verifying if m22, from Eq. 45, reaches zero for both conduction and valence bands. In other words: it is necessary to calculate the wave vector to obtain the *K* matrix for each slice of each layer for each energy value, from the bottom to the top of the well, then multiply all matrices, and, finally, verify if m22 is zero or very close to it. If this is the case, the energy level is a bond state.

To calculate the wave function is necessary the confined energy first guess calculated before. That is only a guess because there is no guarantee in varying the energy that way and to find the correctly bound state. The correct bound state is established when the wave function converges to zero in the final of the barrier for a specific potential profile. This is the boundary condition and it occurs in both bands. So it is necessary to build the wave function and confirm if its end converges or diverges. If diverges, the correct level is found using the bisection method until the convergence condition is established. The built wave functions in different structures and potentials profiles are showed from Figure 6 up to Figure 9.

To conclude the procedure, it is necessary to calculate the potential due to charge distribution, solving the Poisson's Equation and adding it to the potential due to band offset and applied electric field self consistently.

To validate the estimation process, several different structures from literature were solved and the results are in good agreement. Figure 6 and Figure 7 show the conduction and valence bands (light holes) confined energy levels and their respective wave functions of a single step well from (7). The structure consists of two barriers of GaAs (300 Å), one layer of $In_{0.1}Ga_{0.9}As$ (40 Å) and one layer of $In_{0.3}Ga_{0.7}As$ (40 Å), the last two compounding the well. The wave functions were rescaled for visual purposes.

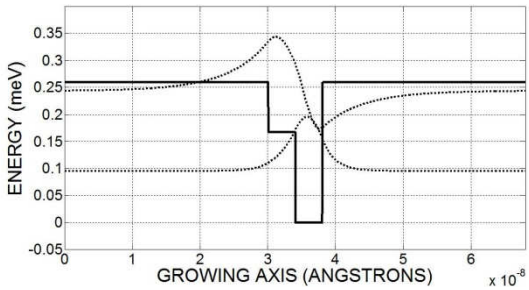

Figure 6: calculated confined energy levels and their respective wave functions of the asymmetric step well studied in **(7)** for conduction band.

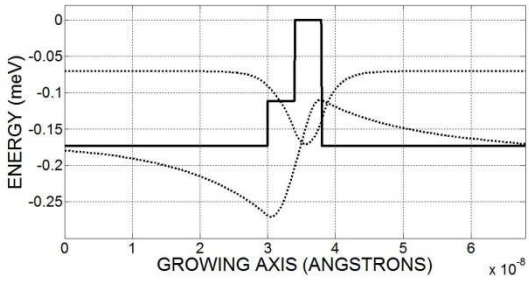

Figure 7: calculated confined energy levels and their respective wave functions of the asymmetric step well studied in **(7)** for light holes.

In this case the error in estimating the confined energy levels is around 15% due to the uncertainties in the used Luttinger parameters and in the band gap estimation, both for InGaAs systems. It indicates the model dependence in these data.

Figure 8 and Figure 9 shows the conduction and the valence (light holes) confined energy levels and their respective wave function of a more complex configuration found in (8). The structure consists of three different-size coupled quantum wells of $In_{0.1}Ga_{0.9}As$ (with length of 55 Å, 100 Å and 150 Å respectively) with barriers of $Al_{0.34}Ga_{0.66}As$ (with length of 100 Å, 15 Å, 15 Å and 100 Å respectively).

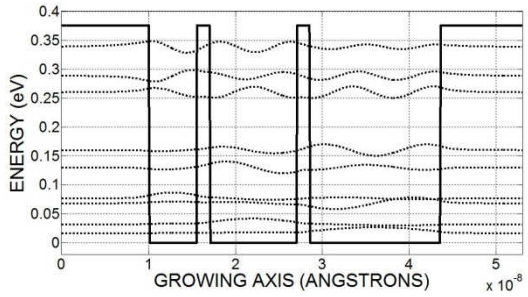

Figure 8: calculated confined energy levels and their respective wave functions of the tri-coupled quantum well studied in **(8)** for conduction band.

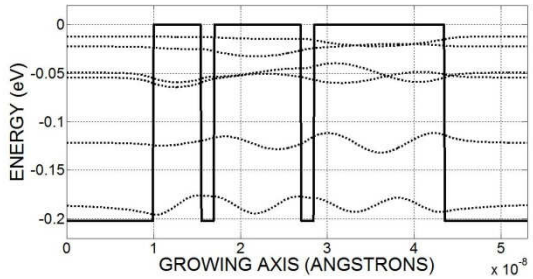

Figure 9: calculated confined energy levels and their respective wave functions of the tri-coupled quantum well studied in **(8)** for light holes.

In this case the error was reduced for less than 10%. The errors are, again, due to the uncertainty in the used parameters and models.

These results show that the TMM may be used in complex structures. For practical devices the effects of the dopants must be considered. Thus, it is necessary to evaluate the charge distribution potential.

The Hamiltonian including the effects of doping and the external applied field can be written as (2)

$$H = \frac{p^2}{2m_0} + V_e(z) - qFz + V_\rho(z) \qquad \text{Eq. 47}$$

where $V_e(z)$ represents the band-offset potential, the second term represents the potential change caused by the applied field *F*, *q* is the electron charge and *z* is the position in the growth direction. $V_\rho(z)$ is the additional potential arising from the charge distribution, ρ, which can be obtained by solving the Poisson's equation

$$\nabla^2 V_\rho = \frac{-\rho}{\varepsilon} \qquad \text{Eq. 48}$$

where ε is the permittivity of the material. One way to determine its solution is to establish the electric field strength. The potential and the electric field are related by

$$V_\rho(z) = -\int_{-\infty}^{\infty} E \cdot dz \qquad \text{Eq. 49}$$

As cited in (2), here, the one-dimensional characteristic of the band edge potential imposes the one dimension charge distribution. As the QW are assumed infinite in *x-y* plane, then any charge density *ρ(z)* can be imagined as an infinite plane, like a *sheet*, with areal charge density *σ(z)* and infinitesimal thickness *δz* (9). The electric field produced by such *charged sheets* is perpendicular to it and given by

$$E = \frac{\sigma}{2\varepsilon} \qquad \text{Eq. 50}$$

The total electric field strength due to many of these sheets or planes of charge is the total sum of the individual contribution, and is given by (9)

$$E(z) = \sum_{z'=-\infty}^{\infty} \frac{\sigma(z')}{2\varepsilon} sign(z - z'), \qquad \text{Eq. 51}$$

where the function sign is defined as

$$sign(z) = +1, z \geq 0; \qquad \text{Eq. 52}$$
$$sign(z) = -1, z < 0$$

and is introduced to account on charge neutrality along the structure.

For a doped semiconductor, there would be two contributions to the charge density *σ(z)*, where the first would be the ionized impurities and the second the free charges carriers. Can be assumed that the former may be obtained from the doping density profile, *d(z)*, and the latter may be obtained from the probability distribution of the carriers in the heterostructure, $(\psi_i^*(z)\psi_i(z)\delta z)$ (2). The net charge density in any of the planes as given by (2)

$$\sigma(z) = q[N\psi_i^*(z)\psi_i(z) - d(z)]\delta z, \qquad \text{Eq. 53}$$

where q is the charge on the extrinsic carriers. When more than one subband is populated, the contribution to the charge density must be summed over the relevant subbands, resulting in (9)

$$\sigma(z) = q\left(\sum_{i=1}^{n} N_i\psi_i^*(z)\psi_i(z) - d(z)\right)\delta z, \qquad \text{Eq. 54}$$

where N_i represents the total number of electrons per unit area in each subband. Mathematically (2),

$$\sum_{i=1}^{n} N_i = N = \int_{all\ z} dz\delta z. \qquad \text{Eq. 55}$$

Re-arranging all the parameters, the final expression of $V_\rho(z)$ is

$$V_\rho(z) = \int_{-\infty}^{z}\left\{\sum_{z'=-\infty}^{\infty}\left[\frac{[\sum_{i=1}^{n} N_i(\psi_i^*(z)\psi_i(z)\delta z) - d(z)\delta z]}{2\varepsilon} sign(z - z')\right]\right\}dz \qquad \text{Eq. 56}$$

where all the parameters are known, except the wave functions, but that are calculated by TMM. Here, δz is the increment used to define the growing axis. For the calculations procedure, since the dopping concentrations in practical devices are not to hogh and

normally the separation between the first excited state and the ground state in QWIPs are greater than $3K_BT$, it is reasonable to assume that all carriers in the QW conduction band are in the ground state, resulting in N_i=N. Finally, can be said that to calculate the confined energy levels and their respective wave functions, the Schrodinger and Poisson equations are solved self-consistently, the latter as a part of the self-consistent solution.

To validate the estimation technique, some data from the literature were used, as well as measurements from actual devices.

It is found in (2) a GaAs-based step well with barriers doped in the middle (modulation doped). The structure is comprised of two barriers with three layers of $Al_{0.44}Ga_{0.56}As$ having length of 90, 95 and 90 Å, respectively. The middle layer is n-doped with $1.8*10^{17}$ carriers/cm^3. The well is formed by one layer of $Al_{0.18}Ga_{0.82}As$ and one layer of GaAs. The results are shown in Figures 10, 11, 12 and 3.

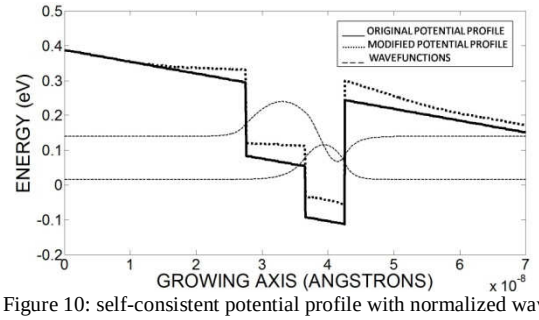

Figure 10: self-consistent potential profile with normalized wave functions for the two lowest energy levels under 30 KV/cm electric field. The solid line is the potential profile with no charge distribution effects, the dotted line is the potential profile including the charge distribution, and the traced lines are the wavefunctions.

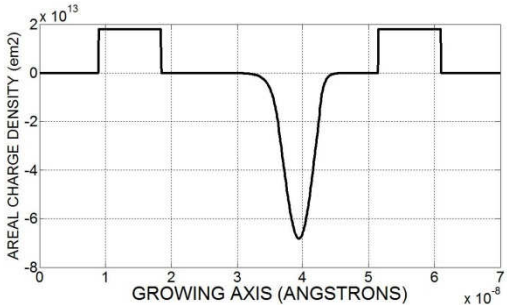

Figure 11: areal charge density profile calculated in the self-consistent procedure.

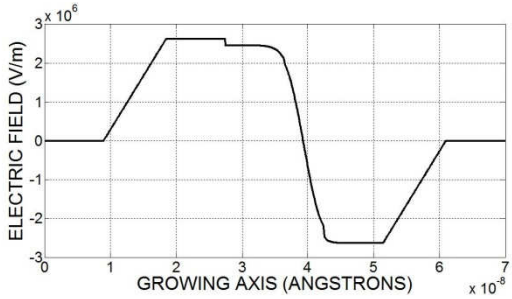

Figure 12: electric field through the structure calculated in the self-consistent procedure.

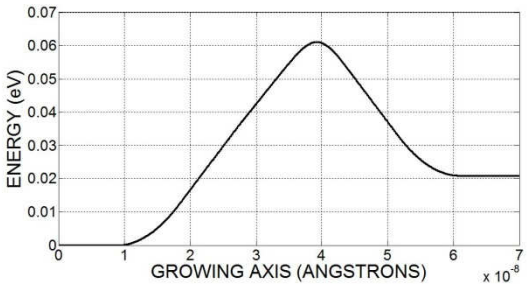

Figure 13: charge distribution potential profile calculated in the self-consistent procedure.

These results show good agreement with (10). The error in estimating the confined energy levels are less than 10% for the calculated confined energy levels, but for the transition between E1-E2 is around 5%.

Some results from the literature were selected in order to compare the estimation obtained by the TMM. Table I shows the comparison measurements reported in the literature and the TMM estimation, where HH, LH, and E represent the confined levels for heavy holes, light holes and conduction band, respectively, and λ_p represents the peak wavelength. The description of the structure are shown in Table 2.

TABLE I: comparison between the literature data and the TMM results.

Reference	Ref. Result	TMM result
(11) Sample E	λ_p = 8.6 μm	λ_p = 8.88 μm
(12) Sample 1	HH1= 6.7 meV HH2=26.6 meV LH1=19.2 meV	HH1= 7.1 meV HH2=28 meV LH1=19 meV
(12) Sample 3	HH1= 9.98 meV HH2=39.3 meV HH3=82.2 meV LH1=27 meV LH2=89.8 meV	HH1= 10 meV HH2=40.9 meV HH3=83.9 meV LH1=26.1 meV LH2=87.3 meV
(13) Sample A	λ_{p1} = 772 nm HH1-EC1 λ_{p2} = 760 Nm LH1-EC1	λ_{p1} = 763 nm HH1-EC1 λ_{p2} = 750 Nm LH1-EC1
(14) Sample A	λ_{p1} = 30.6 μm HH1-LH1 λ_{p2} = 16.4 μm HH1-HH2	λ_{p1} = 41 μm HH1-LH1 λ_{p2} = 16.2 μm HH1-HH2
(15) Sample A	λ_p = 4.3 μm	λ_p = 4.7 μm
(15) Sample B	λ_p = 9.4 μm	λ_p = 9.2 μm

Table II: sample structures from the literature

Reference / Sample	Composition / Barrier Width	Composition / Well Width	Doping
(11) Sample E	$Al_{0.26}Ga_{0.74}As$ 500 Å	GaAs 50 Å	n-type $0.42.10^{18}$ cm^{-3}
(12) Sample 1	$Al_{0.21}Ga_{0.79}As$ 300 Å	GaAs 100 Å	no doping
(12) Sample 3	$Al_{0.21}Ga_{0.79}As$ 300 Å	GaAs 78 Å	no doping
(13) Sample A	$Al_{0.3}Ga_{0.7}As$ 500 Å	GaAs 46 Å	p-type 5.10^{12} cm^{-3}
(14) Sample A	$Al_{0.3}Ga_{0.7}As$ 300 Å	GaAs 40 Å	p-type 4.10^{18} cm^{-}
(15) Sample A	$Al_{0.38}Ga_{0.62}As$ 300 Å	GaAs 5 Å / $In_{0.35}Ga_{0.65}As$ 24 Å	n-type $2.5.10^{18}$ cm^{-3} 2 V bias
(15) Sample B	$Al_{0.27}Ga_{0.73}As$ 500 Å	GaAs 55 Å	n-type $0.7.10^{18}$ cm^{-3} 2 V bias

The error between the estimation and the measurements is less than 5%.

It is important to point out that all the simulated quantum wells are part of a superlattice. Since they are decoupled in the structure, they can be simulated separately.

In the next case, this is used a structure of a real device extensively measured (2) (16). The entire structure is composed by three different QW stacks separated by contact layers, each one responsible to detect in a different band in infrared spectrum. Two of them are analyzed. The first one is responsible to detect the long infrared and it is formed by 20 repetitions of $Al_{0.26}Ga_{0.74}As$ (300 Å)/GaAs (52 Å)/ $Al_{0.26}Ga_{0.74}As$ (300 Å) quantum wells where the GaAs well is $5x10^{17}$ cm^{-3} Si doped (sample A). The second is responsible to detect the near infrared and is composed by 20 periods of undoped GaAs (300 Å)/$In_{0.25}Ga_{0.75}As$ (40 Å)/$In_{0.10}Ga_{0.90}As$ (43 Å)/ GaAs (300 Å) step quantum wells (sample B). They were chosen because show the interband and intersubband transitions.

Table III shows the comparison between the theoretical prediction for the peak wavelength absorbed and the prediction made by the TMM for the same parameter. Figure 14 and Figure 15 show the measured responsivity. All the measurements were done at 10 K.

TABLE III: comparison between the theoretical predictions for peak wave length absorbed (16) and the TMM results.

Reference	Ref. Result	TMM result
Sample A n-type doped	$\lambda_{pE1\text{-}E2}$ = 8.7 μm bias=1 V	$\lambda_{pE1\text{-}E2}$ = 9.2 μm bias=1V
Sample B n-type undoped	$\lambda_{pHH1\text{-}E1}$ = 930 nm $\lambda_{pHH2\text{-}E1}$ = 895 nm $\lambda_{pHH1\text{-}E2}$ = 870 nm $\lambda_{pHH2\text{-}E2}$ = 840 nm $\lambda_{pLH1\text{-}E1}$ = 910 nm $\lambda_{pLH1\text{-}E2}$ = 852 nm bias= 1V	$\lambda_{pHH1\text{-}E1}$ = 979 nm $\lambda_{pHH2\text{-}E1}$ = 930 nm $\lambda_{pHH1\text{-}E2}$ = 895 nm $\lambda_{pHH2\text{-}E2}$ = 854 nm $\lambda_{pLH1\text{-}E1}$ = 956 nm $\lambda_{pLH1\text{-}E2}$ = 875 nm bias= 1V

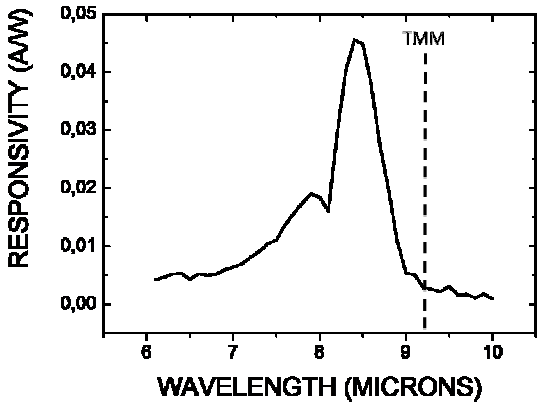

Figure 14. Responsivity of the LWIR quantum well stack at 10 K, for a set of forward bias voltages. The theoretical intersubband transition is indicated by an arrow.

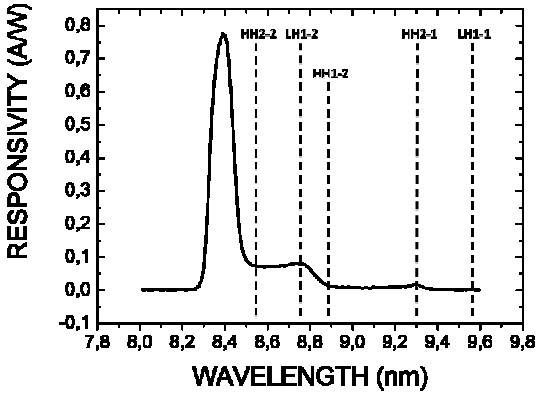

Figure 15: Responsivity of the NIR quantum well stack at 10 K, for a set of forward bias voltages. The theoretical interband transitions are indicated by the arrows **(16)**.

As can be seen in the previous figures, there is a good agreement between the simulated peak wavelength and the measurements, mainly in the Figure 15, where the average error is less than 5% between the wavelength peaks measured and predicted. The difference between estimated results and measurements come from the parameters used in the calculation procedure and the uncertainty inserted in the Varshini's equation used to estimate the semiconductors band gap.

Finally, the results from TMM are compared to the results from the photoluminescence (PL) made in the sample B of the structure described in (17). The PL shows a peak at 0.94 microns for HH1-E1 transition, while the TMM gives 1.06 microns. That is an error around 10%. Again, the difference is behaving likely due to the uncertainties in the band offset parameters.

These results show that the TMM is a suitable technique to calculate the bound states in complex structures, even in asymmetric structures with applied electric field. The results are very dependent from the alloy parameters. Therefore, it is absolutely necessary to work with reliable data.

V. FINAL CONSIDERATIONS

An approach to calculate the bound states in both conduction and valence bands using an analytical solution to a 2x2 Hamiltonian for strained QW was presented. Also, the formalism of TMM to solve the Hamiltonians was presented. Numerical results for AlGaAs / GaAs / InGaAs QW with different molar concentration from the literature were found in good agreement with the used technique.

The TMM approach was used to estimate the peak wavelength absorbed by transitions that occur in actual QWIPs. The comparison presented good agreement between the results and the average error was around 6%.

These results indicate that the TMM technique to find the eigenenergies and the eigenfunctions can be used in QWIP design. The error in some structures due to the alloy parameters uncertainties used to build the potential profile should be reduced

These results indicate that is possible to refine the method and use it towards estimation of QWIP figure of merit that is an important step of QWIP design.

REFERENCES

1. **NAG, B. R.** *Physics of Quantum Wells Devices.* London : Kluwer Academics Press, 2001.
2. **ALVES, F. D. P.** *Three-band Quantum Well Infrared Photodetector using interband and intersubband transitions.* S. José dos Campos : Instituto Tecnológico de Aeronáutica, 2008.
3. **SCHNEIDER, H. and C., LIU H.** *Quantum Well Infrared Photodetector*. Berlin : Springer Series in Optical Sciences, 2007.
4. **CHUANG, S. L.** Efficient band-structure calculations for strained quantum wells. *Phys. Rev. B.* 1991, Vol. 12, 43, p. 9649.
5. **PÉREZ-ALVAREZ, R. and GARCÍA-MOLINA, F.** *Transfer Matrix, Green Functions and Related Techniques.* Castello de la Plana : Publicacions de la Universitat Jaume I, 2004.
6. **VURGAFTMAN, I. and MEYER, J. R.** Band Parameters for III-V compoound semiconductors and their alloys. *J. Appl. Phys.* 89, 2001, Vol. 111, pp. 5815-5875.
7. **THOUSE, M. P. et al.** Near- and mid-infrared bi-periodic grating coupled one- and two-color Quantum Well Infrared Photodetector. *Apllied Physics Letters.* 86, 2005, Vol. 9, p. 93501.
8. **WORKMAN, C. L.** *Intersubband Transitions in strained InGaAs Quantum Well for multi-color Infra-red Photodetector Applications* . Fayeteville : University of Arkansas, PhD Thesis, 2000.
9. **HARRISON, P.** *Quantum Wells, Wires and Dots.* West Sussex : John Wiley & Sons, 2006.
10. **HUANG, F. Y. et al.** Self-consistent simulation of Strak shift of intersubband transition in modulation-doped step quantum wells. *Applied Physics Letters.* 63, 1993, Vol. 12, pp. 1669-1671.
11. **LEVINE, B. F.** Quantum-well infrared photodetectors. *Journal of Applied Physics.* 74, 1993, Vol. 8.
12. **ANDREANI, L. C.** Hole subbands in satrained GaAs-Ga1-xAlxAs quantum wells: exact solution of the effective mass. *Physical Review B.* 36, 1987, Vol. 11.
13. **PALTIEL, Y. et al.** Voltage tunabilty of high performence Zn doped p-type QWIP grown by MOVPE. *Infrared Physics and Technology.* 47, 2005, pp. 37-42.
14. **MAN, P. and PAN, D. S.** Analysis of normal incidence absorption in p-type QWIP. *Applied Physics Letters.* 61, 1992, Vol. 23.
15. **TIDROW, M. Z.** A high strain two-stack two-color QWIP. *Applied Physics Letters.* 70, 1997, Vol. 7.
16. **ALVES, F. D. P. et al.** Widely separete spectral responsivity QWIP using interband and intersubband transitions. *IEEE Sensors Journal.* 8 (6), 2008.
17. **QUIVY, A. A.** *PL MADE IN GROWED HETEROSTRUCTURES.* [email] 2008.
18. **SINGH, J.** *Electronic and Optoelecronic Properties os the Semiconductor Devices.* London : Cambridge University Press, 2001.
19. **JENA, D.** *k.p Theory of Semiconductors.* s.l. : University of Notre Dame, 2004.
20. **LIU, H. C. et al.** p-type quantum well infrared photodetectors covering wide spectrum. *Electronic Letters.* 38, 2002, Vol. 16.